Mojave National Preserve

National Park Service
U.S. Department of the Interior

Sweeney Granite Mountains Desert Research Center

Natural Reserve System
UNIVERSITY OF CALIFORNIA

Science Newsletter

Pre-Eurosettlement Wildfires in Mojave National Preserve

Joseph R. McAuliffe[1]

Ecologists and conservationists generally agree that vegetation in the Mojave Desert does not readily recover after large wildfires. In recent times, when wildfires have occurred in this region, they have often been associated with accumulations of fine fuels produced by non-native ephemeral grasses like red brome (*Bromus madritensis*). Within the last 50 years, such wildfires have caused long-lasting alterations of the shrub-dominated vegetation in some parts of the Mojave Desert (*1-3*).

Before the historically recent spread of non-native grasses, wildfires apparently rarely occurred in the more arid, sparsely vegetated lower elevations of the Mojave Desert. However, that may not be true for some of the less arid portions at higher elevations with denser vegetation. Although it is the smallest of the North American deserts, different parts of the Mojave Desert vary considerably in the amount and seasonality of precipitation. Summer precipitation is common in eastern portions, where Mojave National Preserve (the Preserve) is located, but markedly declines to the west. Higher elevations receive more precipitation than do lower elevations. The Preserve's mountain ranges and uplands including the Clark Mountains, New York Mountains, the Providence

In this Issue:

[1] Desert Botanical Garden. Phoenix, Arizona.

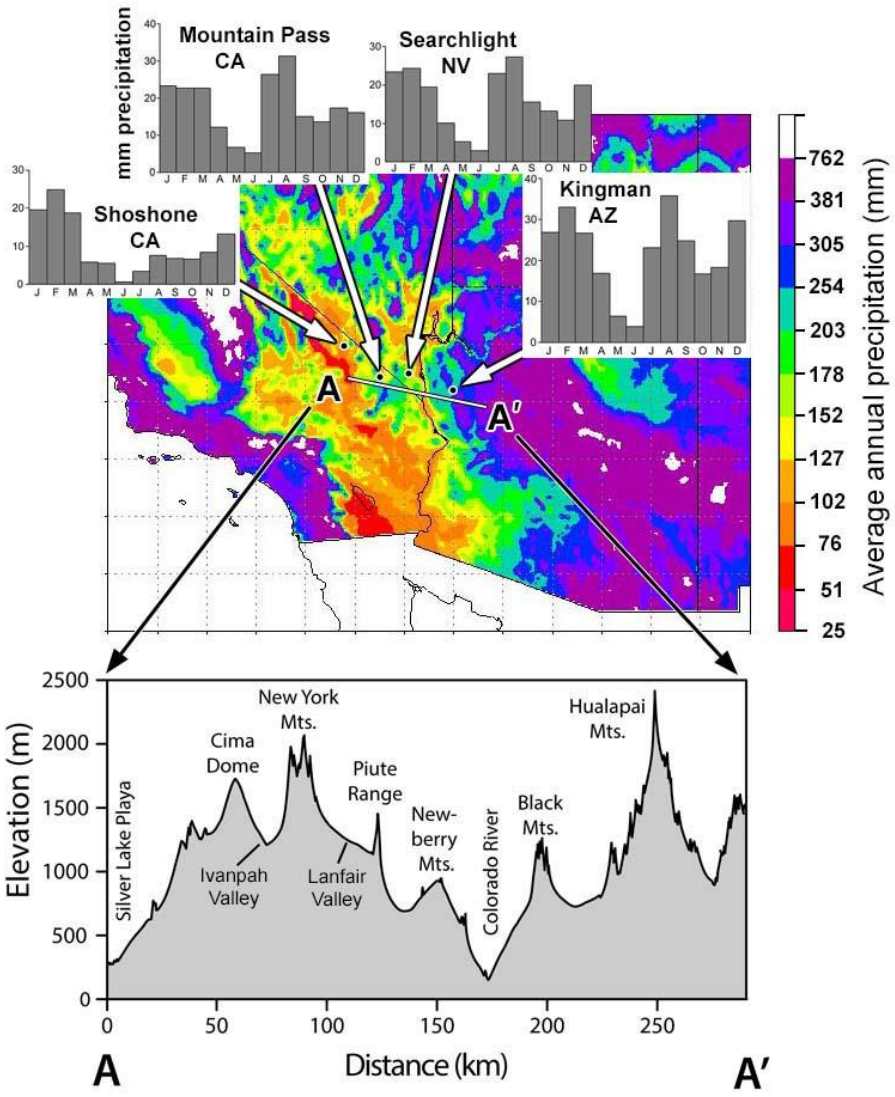

Figure 1.

Top) Modeled average annual precipitation1961-1990 (*20*), modified from an image produced by Western Regional Climate Center (https://wrcc.dri.edu/Climate/precip_map_show.php?map=25). Histograms show average monthly precipitation at four stations along a west-east gradient. The transect A – A' is the location of the topographic cross-section shown in the lower panel.

Bottom) Cross-section showing the prominent topographic bulge of the East Mojave Highlands, including the New York Mountains and Cima Dome, as compared with the arid, lower Colorado River Valley to the east and the long trough containing Soda Lake Playa, Silver Lake Playa, Silurian Valley, and Death Valley to the west and northwest.

Range, and Cima Dome, together with the relatively high basins between them (Lanfair and Ivanpah Valleys), form a regionally elevated topographic bulge that I refer to as the East Mojave Highlands. This area receives substantially greater amounts of precipitation than the surrounding lowlands, including significant summer rainfall (Figure 1). Precipitation during the summer months supports vegetation dominated by native perennial warm-season grasses unlike that found in any other portion of the Mojave Desert (*4, 5*). One of the predominant grass species, black grama (*Bouteloua eriopoda*), is a characteristic species of warm, semi-arid grasslands found throughout southeastern Arizona, New Mexico, and western parts of Texas. The western limit of the distribution of this grass is within the Preserve, in the vicinity of Cima Dome and the Clark Mountains. In the Preserve, landscapes occupied by black grama and several other native perennial grasses occur principally at elevations above 1400 m (4590 ft) and represent the western-most outposts of the warm-temperate "desert grasslands" of the American Southwest (*5*). Joshua trees (*Yucca brevifolia* var. *jaegeriana*) typically stud these landscapes in the lower elevations, and widely spaced Utah juniper (*Juniperus utahensis*) provide an arborescent component in upper elevations, giving the vegetation a savanna-like appearance (Figure 2). Following the removal of livestock in much of the Preserve around 2000, the native perennial grasses have rebounded, and in doing so, have contributed to substantial increases in relatively continuous covers of fine fuels that could potentially carry wildfires (*5*).

Figure 2. Top) *Mojavean juniper savanna*, ~ 1550 m elevation on east side of New York Mountains near New York Mountain Road. Dominant perennial grasses are *Bouteloua eriopoda* and *Hilaria jamesii*. Photograph taken in October, 2018, within survey area described in text. Bottom) *Mojavean Joshua tree savanna*, ~ 1450 m elevation along Ivanpah Road, Lanfair Valley on east side of New York Mountains. Dominant perennial grass in foreground is *B. eriopoda*. Non-native ephemeral grasses are virtually absent, probably due to below-average cool-season precipitation in the preceding winter-spring season. Photograph taken in October, 2014.

The Mojave National Preserve Fire Management Plan (FMP) (*6*) recognized that wildfires probably occurred in pre-Eurosettlement times in vegetation such as this. It was not until the latter decades of the 1800s that livestock ranching and other kinds of land usage began in some places to significantly alter the vegetation (*5*). However, to date there has been no reconstruction of the history of natural fire regimes before that time for the Preserve. Furthermore, little information exists regarding natural wildfire regimes in structurally similar juniper savannas in other parts of the American Southwest (*7*). The 2004 FMP acknowledged the need "…to foster an improved understanding of fire and its role as a natural process through monitoring efforts and scientific research" and that the current lack of information impedes the capacity to develop and implement a fire management policy that may better suit overall NPS goals to restore ecosystems or their components that have been altered in the past by human activities.

The need for knowledge about natural fire regimes in the Preserve prompted a search for evidence of wildfires in pre-Eurosettlement times. I have long been interested in the ecology of semi-arid grasslands of the American Southwest, and my investigations of those in the eastern portion of the Mojave Desert began in 1989 (*5*). During the course of vegetation surveys in the Preserve, I encountered very old stumps of Utah Juniper in several places that bore weathered, fire-hollowed or charred surfaces – evidence of fire at some time long ago. Realizing such stumps could yield information about the timing of past fires, I set out to closely examine this potential evidence. In 2017, I established a 2.6 x

1.9 km survey area in Lanfair Valley within which all remains of fire-scarred juniper trunks would be located and mapped. The area ranges in elevation from 1470 – 1600 m (4820 – 5250 ft) and is bisected by New York Mountain Road near the mouth of Carruthers Canyon (Figure 3A). I divided the area into 29 meridional strips, each 0.001° longitude in width (~ 90 m) and systematically searched each strip for rooted remains of trees bearing evidence of previous fire (e.g., charred or fire-scalloped surfaces & fire-hollowed stumps). I recorded geolocated coordinates of all fire-scarred remains, along with several other attributes regarding the size and condition of the tree. I also recorded any locations of historical artifacts. I completed the survey of the entire area in May 2019 after 33 days of fieldwork and an estimated 500 km of walking back and forth in a tight, zig-zag pattern within the survey strips in search of evidence. The number of old juniper trunks in the area that bore evidence of past fires was surprising: 664 fire-scarred remains of Utah juniper and 10 live trees with fire scars. Each of those records provides unequivocal evidence of the occurrence of fire at that location at some time in the past (Figure 3B). Those remains ranged from nearly completely consumed, fire-hollowed stumps to standing remains of fire-hollowed and charred trunks (Figures 4, 5). Although the remains occurred in most parts of the survey area, they were more concentrated in some areas (Figure 3B).

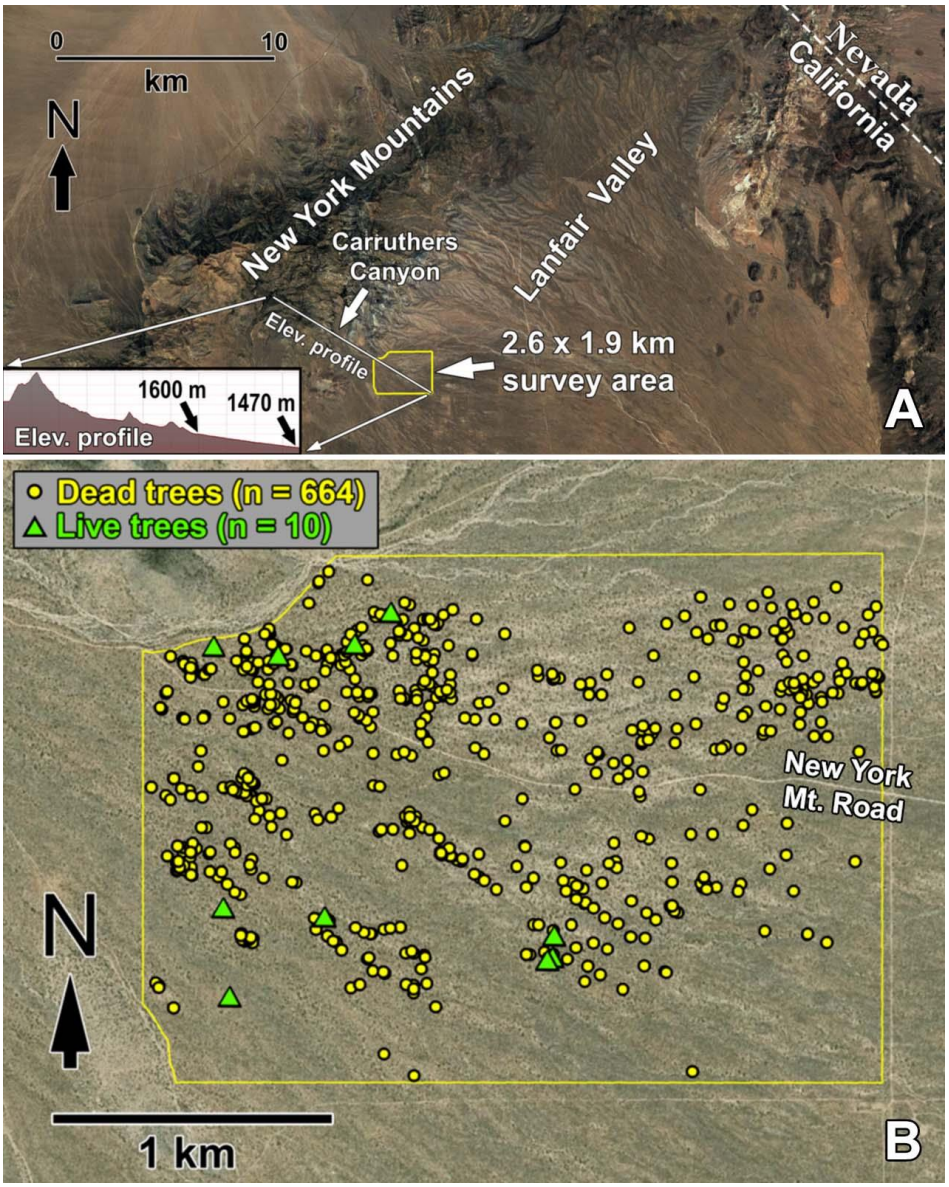

Figure 3. A) Location of survey area on eastern side of New York Mountains within Mojave National Preserve. B) Mapped locations of all fire-scarred dead junipers (yellow dots) and live junipers (green triangles) within the survey area. A total of 674 data points were recorded.

With the fire-scarred remains mapped, determining the timing of past fires posed the next research challenge. The vast majority of remains were extremely weathered, indicating those trees died perhaps a century or more ago. One important clue to the timing of past fires was the widespread occurrence of woodcutting done long ago that was apparently focused on fire-killed trees or branches. Woodcutting was done by axe and within the survey area, I located 846 axe-cut, dead stumps and 158 live trees that had large stems selectively removed by axe. Axe-cut surfaces were extremely weathered, indicating a considerable length of time since the woodcutting occurred. Of the large number of dead, axe-cut stumps recorded at the site, 21 contained axe cuts superimposed directly on fire-scarred surfaces, indicating the woodcutting occurred after the damage by fire (Figure 6). Consequently, knowledge about the timing of wood harvest at the site would help constrain the timing of the wildfires that had occurred earlier.

Historical artifacts found in the study area proved useful in homing in on a timeframe for when the woodcutting likely occurred. I found many cast-off items, including food tins and horseshoes at what were probably overnight encampments. Assuming the woodcutting was done while people were temporarily based at these encampments, the artifacts helped date the timing of woodcutting (Figure 7). The food tins were particularly valuable because they were all of a type called “hole-in-cap” that have a soldered body with a large opening on one end where the food contents were loaded. A metal cap with a small pinhole, which allowed the venting of steam, was then soldered to cover the large opening, and after heating to sterilize the contents, a drop of solder was applied to the pinhole to seal the can. This early form of canning food was replaced starting in 1904 with the more modern “sanitary can” process involving crimp-sealed ends of cans. The exclusive presence of hole-in-cap food tins at the site provides circumstantial evidence that the woodcutting occurred around or before 1900 (*8*), and consequently that wildfires that killed trees

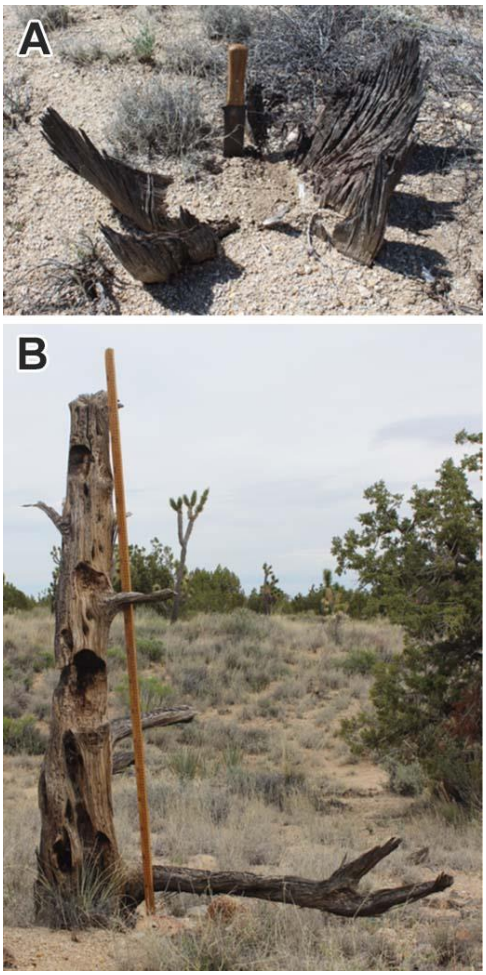

Figure 4. A) Fire-hollowed juniper trunk approximately 30 cm diameter. B) Tall, partially fire-consumed juniper trunk. Height of pole is 2 m.

throughout the site likewise occurred before that time.

The fuelwood was probably cut in the early to mid-1890s to supply mining operations in a short-lived gold mining boomtown called Vanderbilt, located 13 km (8 mi) north of the survey area. Traces of several long-abandoned wagon trails crisscross the study area and one prominent wagon trail leads north from the area of fuelwood harvest toward Vanderbilt. Wood was the only fuel available to power steam engines that drove cable lifts, water pumps, and two large stamp mills in Vanderbilt in 1893-1894 (*9*). The apparent exclusive harvest of dead wood from the study area indicates those operations, which sprung up in a matter of weeks to months, had an immediate and pressing need for large quantities of dry, well-seasoned wood. Those fuel-demanding operations were short-lived and lasted only two to three years.

Although the superposition of axe-cuts on top of fire-scarred surfaces of juniper trunks and the probable use of that wood in Vanderbilt constrains the timing of most wildfires to sometime before the 1890s, more detailed information was sought. Were the fire-scarred trunks the result of a single large fire or have fires repeatedly occurred at the site? If fires repeatedly occurred, how extensive were they? How deep into the past could a record of wildfires be reconstructed? Dr. Scott Abella and Lindsay Chiquoine (Department of Biological Sciences, University of Nevada, Las Vegas) collaborated with me on this project in 2018-19 to explore whether dendrochronological techniques could be used to determine the time of death of individual trees. The approach requires construction of a reliable tree-ring chronology for the site, which is the pattern of tree ring widths over time. However, their analyses of increment cores from large living junipers and the few pinyons from the site indicated that such an approach did not hold promise for two reasons. First, increment growth patterns from tree to tree were not similar enough to enable construction of a chronology and second, few of the living trees sampled were older than 200 years, which eliminated the possibility of using cross-dating techniques to determine the death of trees that died more than 200 years ago (and prior to the era of the Vanderbilt mining), even if a reliable tree-ring chronology could be constructed.

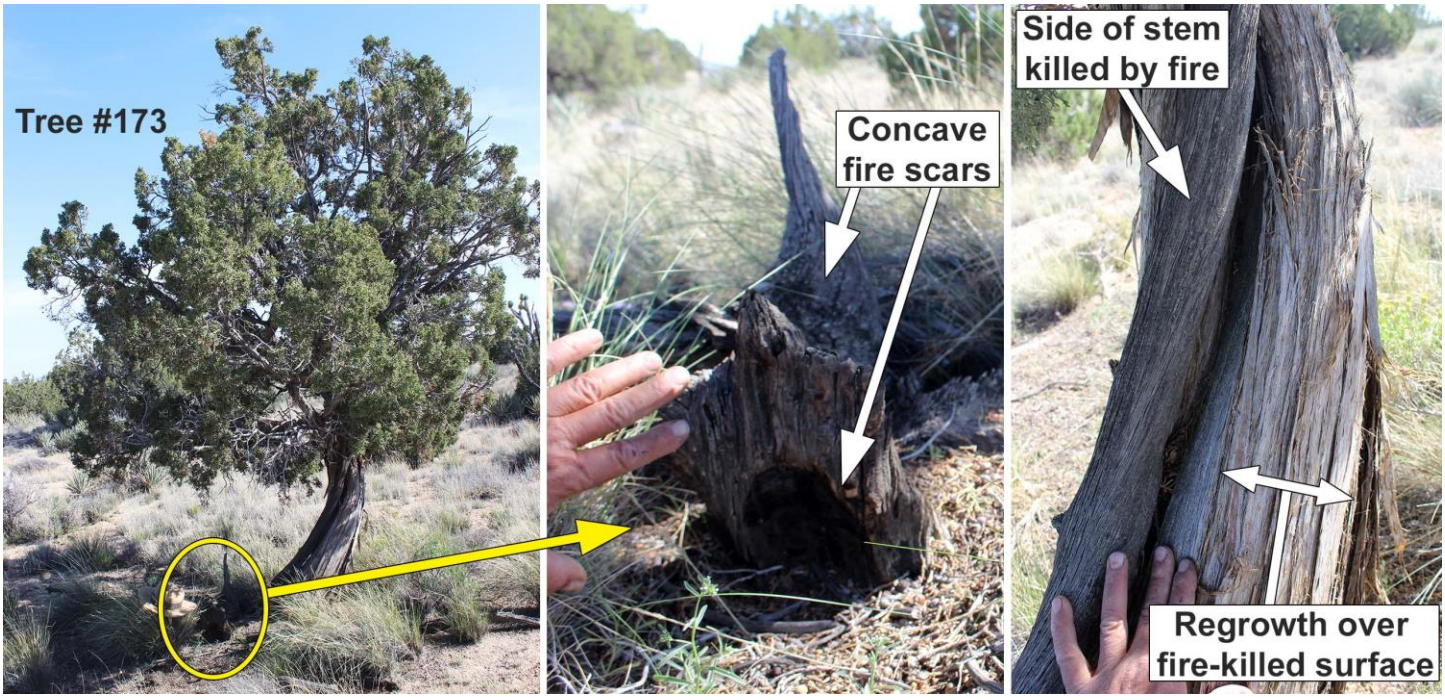

Figure 5. Example of a fire-scarred, surviving tree. The tree was originally double-trunked, one trunk (circled in yellow) was consumed by fire as indicated by concave hollowed fire scars (center). The lower fire scar protected from elements retains the charred surface. The surviving living trunk (right) shows evidence of damage and death of the side of the stem facing the one consumed by fire, but woody regrowth has since enveloped the damaged surface.

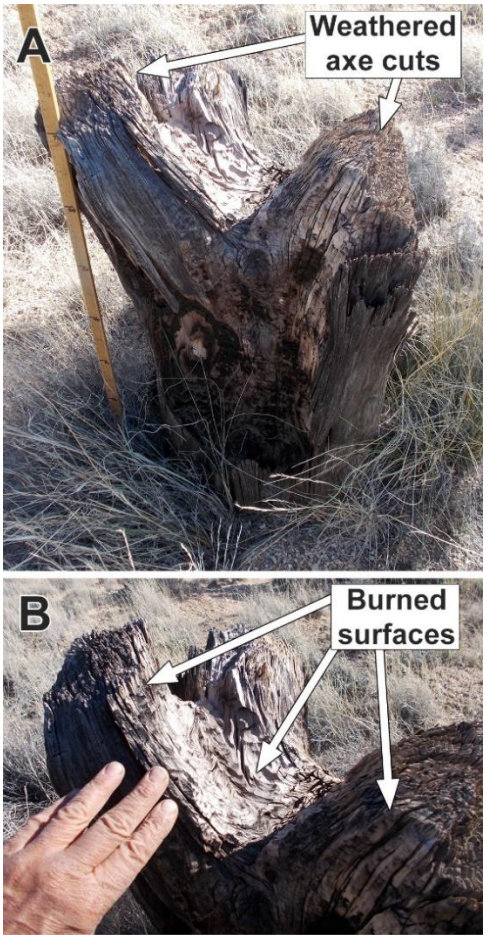

Figure 6. Evidence of woodcutting with axe after the occurrence of wildfire. A) Stump with angled, weathered axe-cut stems. Charred surfaces remain on the lower portion of the trunk protected from the elements. B) Burned surfaces of stem from which charcoal has been removed by weathering have a distinct, scalloped surface. Axe cuts superimposed on those burned surfaces indicate the fire damage preceded the woodcutting.

Since dendrochronological methods were unsuitable, I sought other kinds of evidence on the timing of past wildfires. During the original survey of the site, I recorded large, completely undamaged living junipers with trunks less than a meter away from the remains of four fire-hollowed juniper trunks and stumps (Figure 8). Those large, living trees must have germinated sometime after the fires that completely consumed the trunks of the nearby trees. Therefore, the ages of those living trees would constrain the timing of the earlier fires. In each of the four cases, I took an increment core from the adjacent living tree. Growth ring counts from those cores (excluding apparent false rings) ranged from approximately 200 to more than 325. Junipers may exhibit false rings, missing rings, or incomplete rings, therefore those counts only give approximate ages of those living trees. Nevertheless, the information from the increment cores provided evidence of the occurrence of fires on the order of two or more centuries ago that were capable of entirely consuming the trunks of large juniper trees.

I further investigated the time of death for two of the fire-hollowed stumps by using carbon-14 dating of wood from those stumps. The outermost growth ring of a dead tree represents the last wood produced before death. Radiocarbon dating of the outermost 2 mm of wood from the two stumps indicated the deaths of those trees occurred more than 600 years ago (Figure 8). This timeframe is based on a conservative approach, as the calibrated age ranges of outermost wood of both trees exceeded a century. This lack of precision is because the calibration curve for converting radiocarbon ages into calendar ages frequently departs from linearity, due to variation over time in the production of carbon-14 from nitrogen-14 in the upper atmosphere. These irregularities have been revealed through the precise radiocarbon dating of growth rings of known calendar age from long-lived trees such as bristlecone pine (*10*). In cases where the radiocarbon date of a sample intersects the calibration curve in portions containing these irregularities (e.g., Tree #3029 in Figure 8), the corresponding calendar dates can have very wide ranges of a century or more, or even separate ranges. The long plateau in the calibration curve from 1450 A.D. to the early 1600s and the “wiggles” in the curve from the late 1600s to 1900 A.D. pose the same problems of precise radiocarbon dating of materials from those time periods. The solution to this problem is the application of a specialized technique called carbon-14 wiggle-match dating. In this technique, separate radiocarbon dates are obtained for the wood of the outermost growth

Figure 7. Examples of historical artifacts discovered at encampments in the study area. A-C) Hole-in-cap food tins, which were used exclusively prior to 1904, consisting of a soldered metal cap over a large opening and a central dot of solder to cover a vent hole. D) Cleated horseshoe found in one of the encampment locations. This provides evidence for the use of wagons drawn by draft horses, presumably for transport of the substantial volume of harvested fuelwood needed to run mine operations in Vanderbilt. The slight asymmetry of the shoe (e.g., contrasting widths of right and left sides and ends) indicates a blacksmith-crafted item, rather than a mass-produced shoe.

ring and several additional, widely separated older growth rings, whose numbered sequence is recorded and spans at least several decades. Wood from each ring provides a unique radiocarbon date, and those dates arranged by ring count from the innermost sampled ring to the outermost ring generate a short section of the overall master calibration curve. If that section has a radiocarbon age range and shape that matches a unique position on the calibration curve, the calendar age of the outermost ring can be determined, often with a precision ± 20-30 years. Although this technique does not provide the precision of dendrochronological methods, it can be used in situations like the one in the Preserve where dendrochronological approaches are not feasible. This technique can tolerate missing or false annual rings since the variance in individual radiocarbon dating measurement is typically much larger than those due to inaccuracies in ring-counting. The method has been widely used in archaeological research to date beams, posts, and structural timbers that retain the outermost wood (*11, 12*).

The next phase of this investigation will be the application of carbon-14 wiggle-match dating to more precisely determine the time of death of individual trees. The planned work involves sampling fire-scarred trunks throughout the survey area and will also focus on areas with large concentrations of fire-scarred trunks and snags exhibiting similar degrees of weathering and decay. Samples from those areas will be used to determine whether those remains may have been the result of single fires and also potentially the areal extent of those fires. Since wiggle-match dating requires three or more carbon-14 dates of different growth rings per tree, this will be an expensive approach, as each radiocarbon date costs approximately $400. Funding is currently being sought for this planned future work in order to more fully reconstruct the site's wildfire history.

The preliminary carbon-14 dating discussed above, as well as the circumstantial evidence associated with woodcutting that apparently occurred before 1900 indicates the site has the potential to yield a wildfire history for a 500-year period from around 1400 to 1900 A.D. It is not surprising that wildfires occurred in vegetation

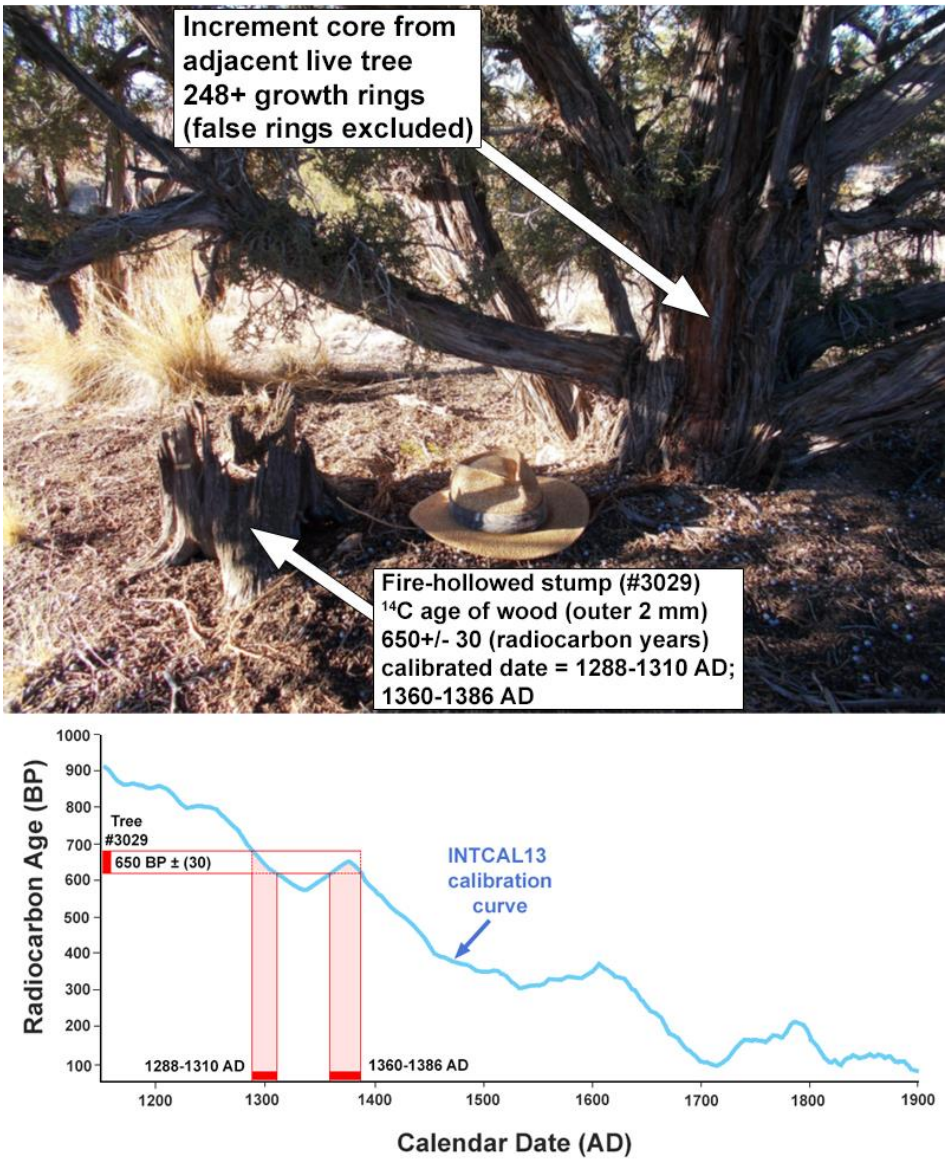

Figure 8. Top) One of four fire-hollowed juniper stumps from survey area positioned next to large, undamaged living junipers. The living tree established after the fire that consumed the adjacent, fire-hollowed stump. In the example above, the living tree had approximately 250 growth rings, indicating more than 250 years had elapsed since the time when the adjacent tree was destroyed by fire. Radiocarbon dating of the outermost wood of the fire-hollowed stump revealed the tree died more than 600 years ago.

Bottom) The INTCAL 13 calibration curve (*10*) is used to apply a calendar age range to radiocarbon dates. In this example (Tree #3029), the radiocarbon date range crosses the calibration curve in two places and therefore provides two potential date ranges: 1288-1310 AD and 1360-1386 AD. This is due to variations over time in the production of carbon-14 from nitrogen-14 in the upper atmosphere, which then cause irregularities ("wiggles" and "plateaus") in the calibration curve. For this reason, a conservative approach was taken in assigning the time of tree death as > 600 ybp.

such as this, where relatively dense stands of perennial grass (Figure 1 Top) would have provided an abundance of fine-fuel that readily carried fire in the right combination of high temperature, humidity, and wind. Lightning associated with summer convective storms is a significant ignition source. Even in modern times, lightning strikes are responsible for the majority of wildfire ignitions in this portion of the Mojave Desert in areas distant from major roads (*13*). In addition to lightning, the aboriginal inhabitants of the region, the Nuwuvi (Southern Paiute) intentionally burned landscapes like these to enhance productivity, to reduce fuel loads within stands of pinyon pine, and for hunting drives (*14*). To the north in the Great Basin, early inhabitants also tended landscapes with fire (*15*) and pre-Eurosettlement wildfire regimes were a

product of interactions of fuel loading, and at least partly, intentional burning by humans (*16*). Such intentional burning in the past probably also occurred in the landscapes with dense perennial grass cover in the *East Mojave Highlands*.

The NPS recognizes fire (either unplanned wildfire or intentional planned ignitions) as a potential management tool for protecting or restoring natural processes and ecosystems. However, such use must be well supported and justified with the best scientific information available (*17*). Livestock grazing beginning in the 1890s through the 20th century produced marked vegetation changes in parts of the Preserve (*5*). Descriptions of the landscape by Lieutenant A. W. Whipple during his 1853-54 expedition to explore a potential route for a transcontinental railroad provide a glimpse into the past of how the vegetation may have once appeared. That expedition travelled directly across Lanfair Valley from east to west, from Paiute Springs to Rock Springs, then through Cedar Canyon. Whipple's daily written accounts consistently describe the grassland-like nature of this area (*18*):

March 4, 1854: *"The great plain which our route traversed was founded to be covered with good grass."*

March 5: *"Parsing over the prairie, nearly seven miles west, we arrive at a spring of water oozing from a rocky ravine."* [= Rock Springs}

March 6: *"The hill-sides and ravines are covered with excellent grass."* [referring to the route through Cedar Canyon]

March 7: *"This country affords excellent grazing lands, similar to, but less extensive than those of New Mexico. The grass is highly nutritious."*

In some cases, wildfire contributes significantly to the restoration of landscapes where the original grass-dominated vegetation has been altered by livestock, and this beneficial influence of recent wildfires has been documented at several locations in the Preserve (*5*). Although the 2004 FMP for the Preserve recognized the potential role of fire as a tool in ecological restoration, such use was not included in that plan "…due to the lack of available information regarding the natural fire regime and the extent to which that fire regime has been altered by human activities" (*6*). Consequently, the current fire management plan for the Preserve calls for rapid suppression of all wildfires, regardless of the cause of ignition (*6, 19*).

The wildfire history that this study aims to produce will provide essential knowledge to help inform future wildfire policy and management decisions for the Preserve. Multiple considerations, including the protection of human life and property, cultural sites, as well as populations of native plants and animals, govern decisions regarding wildfire policy in the Preserve and other National Park Service holdings. The knowledge created by this research can also provide a solid foundation for creating interpretive materials for the general public regarding the history of wildfire in the Preserve. Developing and sharing this information will help generate public support for fire management policies, particularly if there are any changes of policy in the future.

References

1. M. L. Brooks, J. R. Machett, Plant community patterns in unburned and burned blackbrush (*Coleogyne ramossisima* Torr.) shrublands in the Mojave Desert. *Western North American Naturalist* **63**, 283-298 (2003).
2. K. J. Horn, J. Wilkinson, S. White, S. B. St. Clair, Desert wildfire impacts on plant community function. *Plant ecology* **216**, 1623-1634 (2015).
3. K. J. Horn, S. B. St. Clair, Wildfire and exotic grass invasion alter plant productivity in response to climate variability in the Mojave Desert. *Landscape ecology* **32**, 635-646 (2017).
4. H. B. Johnson, in *Plant Communities of Southern California*. J. Latting, ed. (Calif. Native Plant Soc. Spec. Publ. No. 2), pp. 125-164 (1976).
5. J. R. McAuliffe, Perennial grass-dominated plant communities of the eastern Mojave Desert region. *Desert Plants* **32**, 1-90 (2016). https://repository.arizona.edu/handle/10150/622004.
6. National Park Service, *Mojave National Preserve Fire Management Plan*. U.S. Dept. of the Interior (2004).
7. W. H. Romme, C. D. Allen, J. D. Bailey, et al., Historical and modern disturbance regimes, stand structures, and landscape dynamics in piñon-juniper vegetation of the western United States. *Rangeland Ecology & Management* **62**, 203-222 (2009).
8. J. C. Horn, *Historic Artifact Handbook*. Alpine Archaeological Consultants, Inc., Montrose, Colorado (2005). http://www.alpinearchaeology.com/cms/wp-content/uploads/2010/01/Historic-Artifact-Handbook.pdf
9. Multiple articles from 1893-1894 in *The Needles Eye*, a newspaper published in Needles, California. Photocopies of originals compiled by L. Vredenburgh and available online: http://vredenburgh.org/mining_history/pdf/NeedlesEye1893-1894.pdf
10. P.J. Reimer, E. Bard, A. Bayless, et al., IntCal13 and Marine13 radiocarbon age calibration curves 0–50,000 years cal BP. *Radiocarbon* **55**, 1869-1887.
11. M. Galimberti, C. B. Ramsey, S. W. Manning, Wiggle-match dating of tree-ring sequences. *Radiocarbon* **46**, 917-924 (2004).
12. C. Tyers, J. Sidell, J. Van der Plicht, P. Marshall, G. Cook, C. B. Ramsey, A. Bayliss. Wiggle-matching using known-age pine from Jermyn Street, London. *Radiocarbon* **51**, 385-396 (2009).
13. M. L. Brooks, J. R. Machett, Spatial and temporal patterns of wildfires in the Mojave Desert, 1980-2004. *Journal of Arid Environments* **67**, 148-164 (2006).
14. B. J. Lefler, M.S. thesis, Portland State University (2014). https://pdxscholar.library.pdx.edu/cgi/viewcontent.cgi?article=3007&context=open_access_etds
15. J. McAdoo, B. W. Schultz, S. R. Swanson, Aboriginal precedent for active management of sagebrush-perennial grass communities in the Great Basin. *Rangeland Ecology and Management* **66**, 241-253 (2013).
16. S. G. Kitchen, Climate and human influences on historical fire regimes (AD 1400-1900) in the eastern Great Basin (USA). *The Holocene* **26**, 397-407 (2016).
17. National Park Service, *Management*

Policies. U.S. Dept. of the Interior (2001). https://www.nps.gov/goga/learn/management/upload/2001-Management-Policies.pdf

18. G.A. Foreman (ed.), *A Pathfinder in the Southwest – The Itinerary of Lieutenant A.W. Whipple During His Expedition for A Railway Route from Fort Smith to Los Angeles in the Years 1853 & 1854*. University of Oklahoma Press, 298 pp. (1941).
19. CDIFP (California Desert Interagency Fire Program), *Fire Management Plan*. 93 pp. (2018).
20. C. Daly, R. P. Nielson, D. L. Philips, A statistical-topographic model for mapping climatical precipitation over mountainous terrains. *Journal of Applied Meteorology* **33**, 140-158 (1994).

Acknowledgements

Drs. Marti Witter and Debra Hughson of the NPS and James Gannon, Bureau of Land Management have all encouraged the continuation and funding of this project. Dr. Scott Abella and Lindsay Chiquoine contributed with their expertise in tree-ring analysis and Veronica Nixon of the Desert Botanical Garden assisted with GIS mapping. Laura Misajet, Exec. Director of the Mojave Desert Heritage and Cultural Association and board member Larry Vredenburgh provided valuable information and access to historical archives. Special thanks is due Dr. Greg Hodgins, Director of the Univ. of Arizona Accelerator Mass Spectrometry Laboratory, for information on the application of carbon-14 wiggle-match dating. Dr. Tasha La Doux encouraged the author to contribute this article and three anonymous reviewers provided helpful suggestions for improving the original manuscript. The Desert Botanical Garden has generously supported this research, including the costs of fieldwork and preliminary carbon-14 dating.

Using Gravity to Map Faults and Basins in the Mojave Desert, California

Victoria E. Langenheim [1]

The Mojave Desert hosts a complex landscape consisting of valleys filled with geologically young deposits and by hills and mountains that are underlain by a diverse assemblage of older, consolidated bedrock. This landscape is sliced up by a broad zone of faulting called the Eastern California Shear Zone (Figure 1). This shear zone has produced a number of large earthquakes in historic time, most notably the 1992 magnitude-7.3 Landers and 1999 magnitude-7.1 Hector Mine earthquakes (*1, 2*). These earthquakes occurred along separate faults of the shear zone that were at the time unmapped or considered to be too small and discontinuous to cause large earthquakes. Two important factors for assessing the seismic hazard of a fault include knowledge of how long it is and how fast it slips, also called the slip rate. Fault length and slip rate determine size and frequency, respectively, of earthquakes. For example, the San Andreas fault, which forms the southwest margin of the Mojave Desert (Figure 1), is such a hazardous fault because it has high slip rate and stretches much of the length of California. Because many of the faults in the Eastern California Shear Zone are in places concealed by young deposits, such as eolian sand (windblown) or alluvial deposits (sediment deposited by water), their entire extent cannot be mapped by examining geologic units exposed at the surface. A third factor for assessing seismic hazard is characterizing the thickness and 3-dimensional (3-D) geometry of geologically young basin deposits, which can enhance shaking not only from a nearby earthquake, but also from a distant earthquake. For example, computer simulations of a large earthquake on the San Andreas fault from the Salton Sea south of Palm Springs to the Mojave Desert predicts very strong shaking in the Los Angeles area because it sits on a very deep basin filled with sediments (*3*). The 3-dimensional geometry of young basin sediments is also important for modeling the movement of groundwater as these young alluvial, fluvial (river), and eolian deposits form the principal aquifers in the Mojave Desert. These deposits

[1] U.S. Geological Survey, Moffett Field, California.

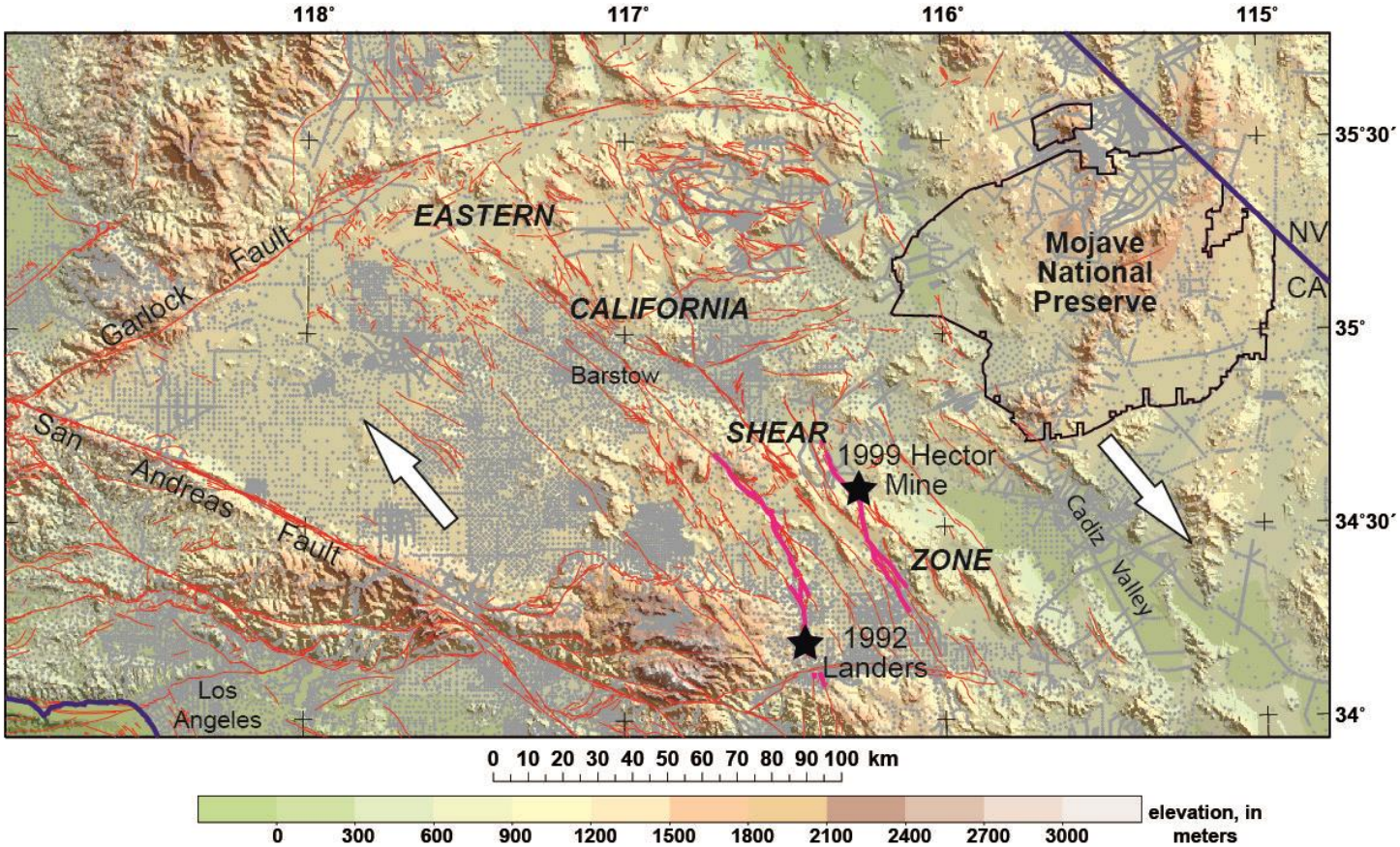

Figure 1. Shaded-relief topographic map depicting a portion of the Mojave Desert showing faults (red lines) of the Eastern California Shear Zone (*12, 13*) and fault ruptures (thick magenta lines) and epicenters (stars) of the 1992 Landers and 1999 Hector Mine earthquakes (*1, 2*). Gray dots are locations of gravity measurements (*6, 7*), which are unevenly distributed throughout the region. The large white arrows show the direction of relative motion across the shear zone.

often make good aquifers because of their high porosity (pore space to hold water) and permeability (connected pore spaces so water can move). Coarser-grained sediments allow better water storage and flow more easily than finer-grained materials, whereas clays retard water flow and form aquitards, the opposite of aquifers. Faults can affect groundwater movement as they can form barriers to movement because of the reduction in grain size within fault zones (*4*) or because they juxtapose deposits of differing permeability. In fact, springs are often found along faults, such as the San Andreas fault and those of the Eastern California Shear Zone.

Thus, knowledge of the 3-D shape of basins is critical for seismic and hydrologic studies. Historically, drilling wells was the best way to gain this knowledge, yet it is expensive and disruptive, and only provides information at one specific, discrete site. However, remote sensing methods that utilize differences in physical properties of rocks and sediments can aid in estimating the shape of basins and mapping fault locations. These methods are non-invasive and provide information across much broader geographic areas than can a single well. In the Mojave Desert, one of these methods, the gravity method, has been applied to characterize basins filled with Quaternary and Neogene (< 23 million years) deposits since the 1950s (*5-7*), as reflected by >28,000 gravity measurements in the region (Figure 1).

How does the gravity method work? It takes advantage of the difference in rock density, such as the contrast between low-density Neogene and Quaternary deposits and the underlying high-density bedrock. The force of gravity is proportional to mass, as per Isaac Newton's famous equation, and density is simply mass divided by volume. Thus, the force of gravity, or what geophysicists measure as the acceleration of gravity (**g**) due to Earth's mass (ME), is related to density within Earth, depending on where one measures that acceleration (Figure 2). However, it is not that straightforward because **g** is also inversely related to the distance squared from the center of Earth (r^2 in Figure 2); Earth is a slightly flattened sphere so one is closer to the center of Earth at the poles than at the equator. Earth's

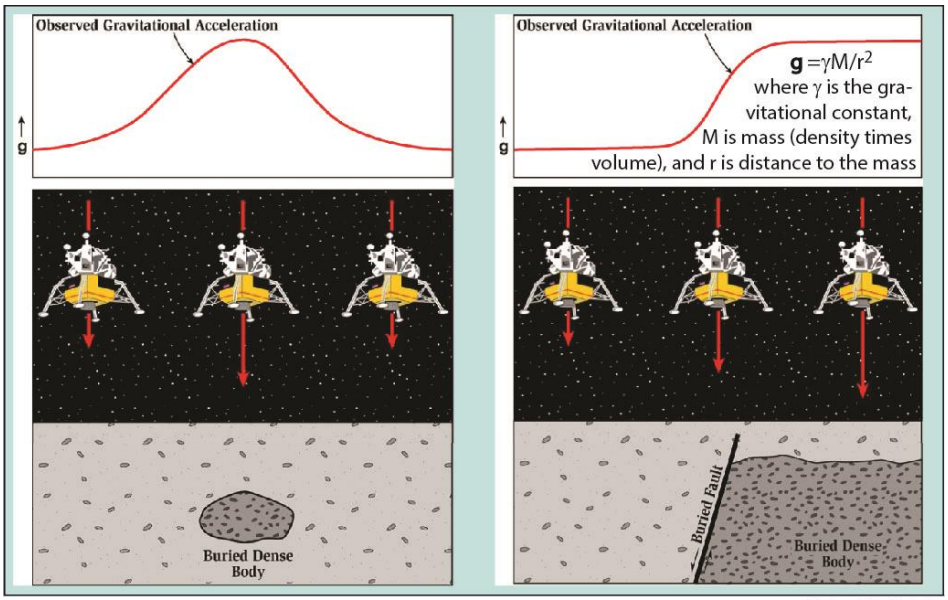

Figure 2. Cartoon showing how gravitational acceleration varies from place to place because of concealed masses beneath the ground surface, all other factors held constant. The lunar lander is pulled more strongly in the area of the dense bodies.

rotation also affects **g** because of centrifugal forces. Even adjacent mountain ranges and the subsurface low-density roots of those mountain ranges affect **g**. Not only does **g** vary from place to place on Earth's surface, but **g** also varies with time because of lunar and solar gravitational forces, the same forces that cause ocean and solid-earth tides (the land surface moves with the tides, with amplitudes of about a meter). Thus, a point measurement of **g** is the total of the pull from masses (density distribution) within Earth as well as the masses of the sun and the moon. All of these effects on **g** can be predicted quite accurately except for those caused by density variations in Earth's crust. To isolate the part of a gravity measurement that reflects the density structure of Earth's crust, these other effects are calculated and subtracted from **g** (*8*) such that the resulting value, or isostatic gravity "anomaly", mostly reflects density variations in the upper 10-15 km of the crust. This anomaly is especially useful in the Mojave Desert because it is sensitive to the depth range of the crust where nearly all of historic earthquakes are located and where groundwater is found.

How does one measure gravity? As one may remember from high school physics, one measures how fast a mass falls; the acceleration of gravity, **g**, is about 32 ft/s^2 or 9.8 m/s^2, often referred to as the standard acceleration of gravity. Acceleration is often expressed in units of Gal (named in honor of Galileo), which is 1 cm/s^2; anomalies caused by crustal geology are usually reported in units of milliGals (mGal), where 1 mGal equals 0.001 Gal. Standard gravity is then 980 Gal or 980,000 mGal. Gravity meters can measure to a precision of 0.001 mGal, which is within one part in one billion of standard gravity. Nearly all the gravity measurements in the Mojave Desert were accomplished using instruments that measure the relative change in **g** from place to place, rather than the absolute value of **g**. These gravity meters are generally more robust, lighter, and more portable (Figure 3) than those that measure the absolute value of **g**. Rather than measuring how fast atoms fall in a vacuum, relative gravity meters measure the stretch on a weighted spring. The changes in spring length for a given gravity meter need to be calibrated by measuring at locations where **g** is already known. The instrument shown in Figure 3 uses a quartz spring. The process of converting relative g measurements to absolute **g** values involves measuring relative **g** at a location of unknown gravity and then moving the gravity meter to a location of known absolute **g** and measuring relative **g** there. The difference in relative **g** readings between the unknown and known locations can be added to or subtracted from the known absolute **g** to then give absolute **g** at the unknown location.

How large are the gravity anomalies due to density variations of the underlying rocks? Values of **g** in the area around Mojave National Preserve vary by nearly 520 mGal (*7*). After these measurements have been processed to remove all the known effects on **g**, the resulting isostatic gravity anomalies vary by no more than 70 mGal (Figure 4). In general, lower gravity anomaly values coincide with Neogene and younger basin fill deposits, as expected because they are typically unconsolidated and have lower density. However, anomaly values can vary significantly for measurements made on bedrock as well. For example, within Mojave National Preserve, values vary as much as 30 mGal between measurements on exposed bedrock in the ranges adjacent to Soda Lake versus those measured near Cima. Across the New York Mountains gravity anomaly values increase northeastward by more than 15-20 mGal, reflecting the density contrast between Precambrian rocks and less dense Cretaceous granitic rocks. In places, the gravity variations on bedrock are as large as or larger than those arising from variations in the thickness of young overlying basin deposits.

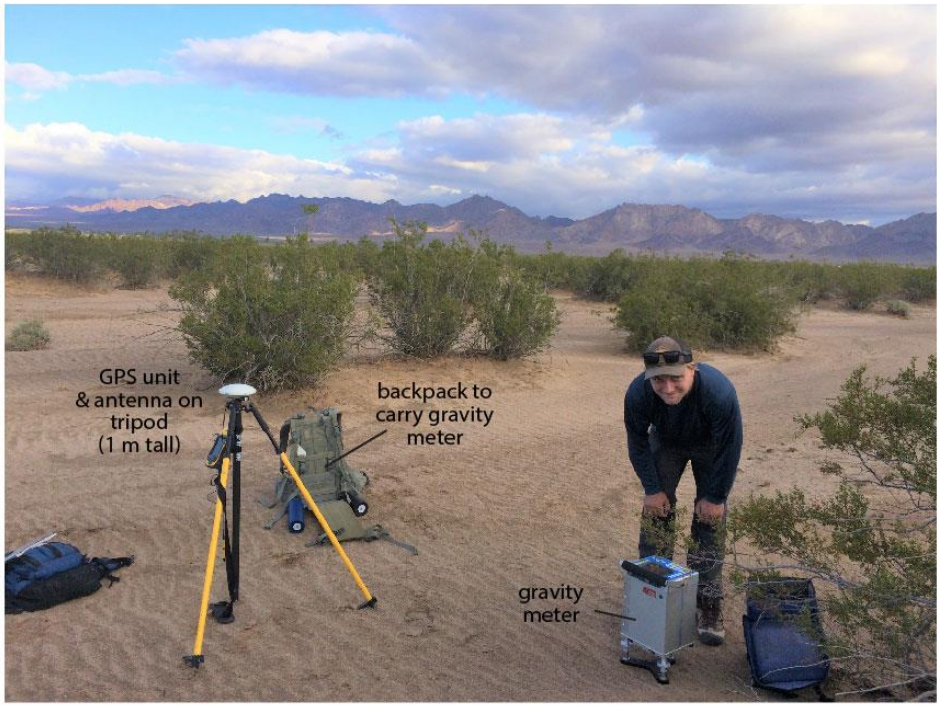

Figure 3. Measuring gravity near Chambless, California, November 2019. View is north towards the Marble Mountains. Gravity meter is leveled so that the maximum value of gravity is measured. A Global Positioning Unit measures elevation accurate to less than 1 ft (0.3 m). These measurements are non-intrusive, leaving no trace.

One technique to estimate thickness of basin deposits (Figure 5) utilizes the mapped geology to separate the gravitational effects of bedrock density variations from those arising from variations in the basin thickness (*9*). The technique basically computes the gravity anomaly at each location based on inputs of density contrast between bedrock and basin fill and the geometry of the basin (width, depth, shape). It is an iterative process because the gravity anomaly arising from the basin deposits affects the gravity measurements made on bedrock (blue dots in Figure 5) near the basin-bedrock interface. The user iterates by calculating the effect of basin-fill deposits on the bedrock gravity anomaly until the modeled gravity anomaly matches the observed anomaly. Another technique uses the horizontal gravity gradient (the change in gravity value over distance) to locate the edges of features that have different densities (*10*), such as faults that juxtapose basin fill against denser bedrock. The gradient is highest over near-vertical contacts between bodies of differing density. The maximum horizontal gravity gradient can not only locate the position of the density contrast but also provide information of the dip (angle projected into the subsurface) of that density contrast (Figure 6).

We applied both techniques in our efforts to better map the easternmost faults of the Eastern California Shear Zone. Geologists had mapped and inferred the locations of discontinuous traces of the Soda-Avawatz fault, projecting southeast towards faults mapped in the Bristol Mountains and Granite Mountains (red lines in Figure 7). Our results highlight the utility of the gravity method in that we now have evidence that the Soda-Avawatz and Bristol-Granite Mountains faults are connected. Furthermore, various studies have postulated a wide range in the amount of slip accumulated over the lifetime of these faults, from as low as 4 km to as much as 45 km (*11*). Clearly, more data are needed to get a clear understanding of the total displacement over time (slip rate) along these faults.

Both Soda-Avawatz and Bristol-Granite Mountain fault zones are marked by prominent gravity gradients, leading to a better understanding of fault lengths and connections. Using our gravity data combined with previously mapped and inferred fault traces, we can see that the northernmost segment of the Soda-Avawatz fault coincides with a gravity gradient (G1 in Figure 7) and as the mapped fault trace continues to the south towards other mapped traces in the Soda Mountains, it projects across a gravity low (L1), which we interpret as a basin formed by concealed fault strands. The margins of the gravity low are parallel to the mapped fault traces that cut bedrock in the Soda Mountains, which are marked by a subtle gravity gradient with denser rocks on the east side of the mapped trace (G2). South of the Soda Mountains in the Soda Lake area, the fault is not mapped at the surface, but its projection to the southeast coincides with a gravity gradient (G3) that marks the northeast margin of a pronounced gravity low (L2). The southwest margin of the gravity low is aligned with bedrock traces of the Bristol-Granite Mountains fault mapped in the northern Bristol Mountains, also coincident with a gravity gradient (G4). We interpret the gravity low as a basin bounded by fault strands of the Soda-Avawatz fault zone.

The Bristol-Granite Mountains fault is also particularly well expressed by a gravity gradient

(G5) between mapped traces in the Bristol Mountains and those mapped along the southwest margin of the Granite Mountains. This 20-km-long gravity gradient is caused by the juxtaposition of lower-density Neogene volcanic rocks to the southwest of the fault and denser granitic rocks to the northeast. Interestingly, at the southern end of the gravity gradient near the northern end of the Marble Mountains (G6), denser rocks to the southwest are next to less dense rocks to the northeast along a distance of approximately 25 km. Farther southeast, the density of rocks again changes across the gravity gradient along the southwest margin of the Marble Mountains (G7) and forms the northeast margin of a prominent gravity low (L3). The gravity gradients indicate that the discontinuous mapped fault strands are connected, albeit concealed beneath the ground surface. The pattern of gravity highs and lows on the southwest side of the fault (1 and 2 in figure 7) can be related to the pattern of gravity highs and lows on the northeast side of the fault (1' and 2' in figure 7) if we move the northeast block 15-17 km to the northwest along the fault. This exercise provides an estimate of long-term offset, that is important for understanding the slip rate on this stretch of the fault zone.

Our gravity data, along with the mapped geology and information from magnetic anomalies, another geophysical dataset that is sensitive to crustal magnetic properties, provide evidence that the Soda-Avawatz and Bristol-Granite Mountains faults are connected and thus is a much longer fault zone. Furthermore, the Bristol-Granite Mountains fault may extend farther southeast than traces mapped at the surface indicate (G7 in Figure 7). Both faults consist of strands that step right. Those areas where overlapping fault strands step to the right coincide with gravity lows that are elongated in a northwest-southeast direction. Using the basin modeling approach illustrated in Figure 5, the gravity lows (L1, L2, and L3 in Figure 7) are caused by basin-fill deposits that are 1-1.5 km deep (Figure 7a). Elsewhere basin-fill deposits are thin (< 500 m), with implications for groundwater exploration in this part of the Mojave Desert.

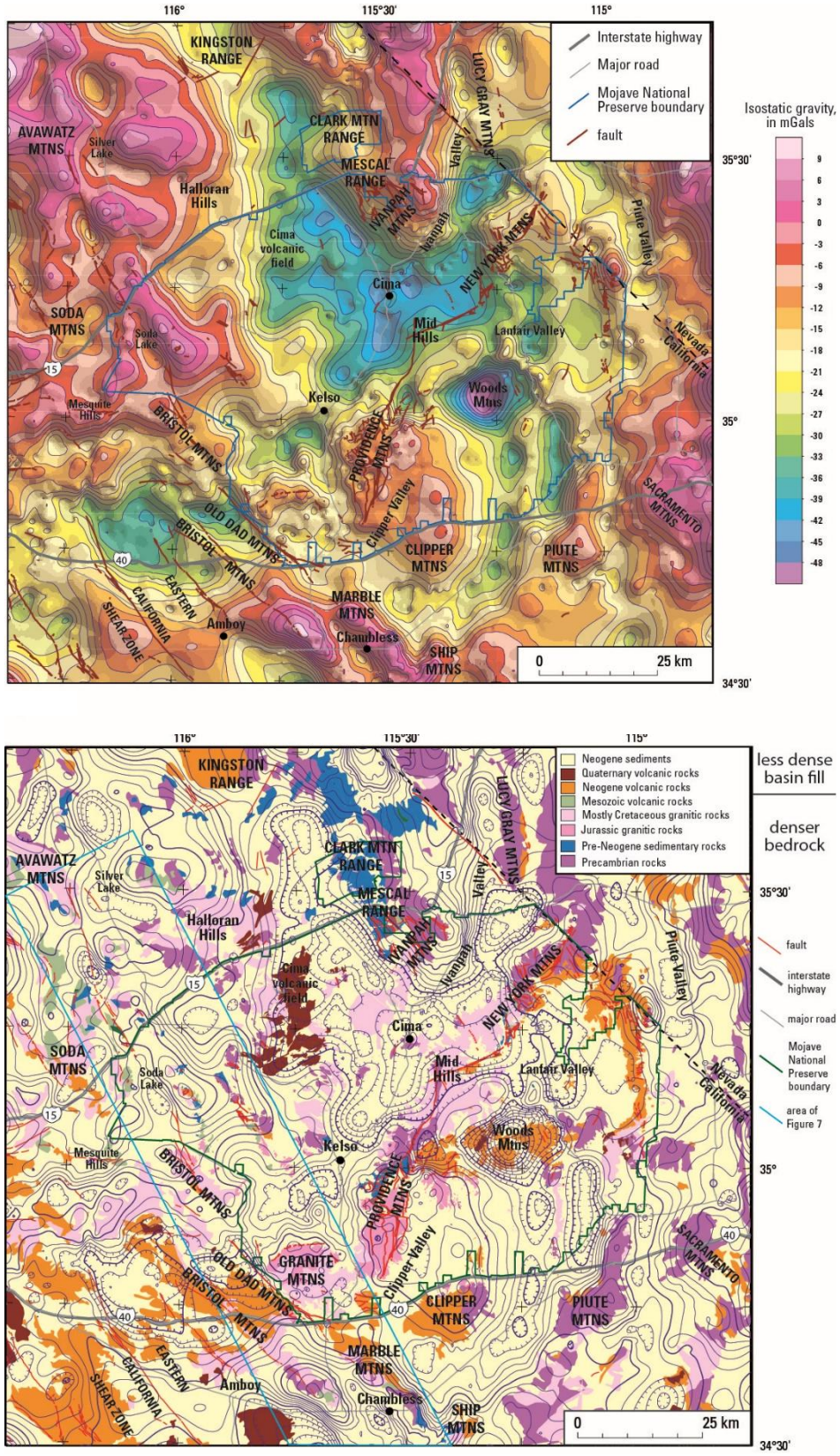

Figure 4. Isostatic gravity anomaly maps of Mojave National Preserve and vicinity (*7*). Top) Anomaly variations shown as color contours. Interval, 3 mGal. Bottom) Same gravity contours shown as dark blue lines superposed on simplified geologic map (*14, 15*). Teeth on contours indicate lows.

Right steps in overlapping strands of a right-

lateral fault (this means that the relative displacement of the block on the other side of the fault is to the right) should produce subsidence that results in formation of a basin. The length of the basin can serve as a proxy for the amount of right-lateral offset on the fault and thus provide information on the long-term slip rate of the fault. The lengths of the basins formed in the Soda-Avawatz and Bristol-Granite Mountains fault zones suggest that the amount of offset decreases from about 17 km near the Marble Mountains at the southern end of the fault zone, to about 8 km near the Avawatz Mountains at the northern end of the fault zone. One explanation for the decrease in offset is that slip is somehow transferred to adjacent faults, such as the east-striking fault in the Bristol Mountains and/or the more westerly striking fault in the Old Dad Mountains. Alternatively, movement along the faults in the northern part of the fault zone may have initiated later than did the faults to the south. More information on the timing of slip along the fault zone is needed to address these questions.

Although gravity, geology, and other geophysical methods have shown that the Soda-Avawatz and Bristol-Granite Mountains fault zones are connected, where the fault zone projects to the southeast into Cadiz Valley is the subject of ongoing studies. Cadiz Valley (Figure 1) forms a broad alluvial expanse, covered in places by sand dunes, with few roads to facilitate access except for the northern part of the valley, which is being developed for agriculture. Efforts to augment gravity measurements in Cadiz Valley can help address where and how this slip is connected to the San Andreas Fault. As we learn more about the fault system in this region, we gain a better understanding of the potential seismic hazards. Gravity anomaly modeling and analysis often lead to multiple interpretations. However, when combined with mapped geology, well data, and other geophysical techniques, gravity data and modeling provide powerful constraints on locations of faults and geometries of basins in the Mojave Desert and elsewhere.

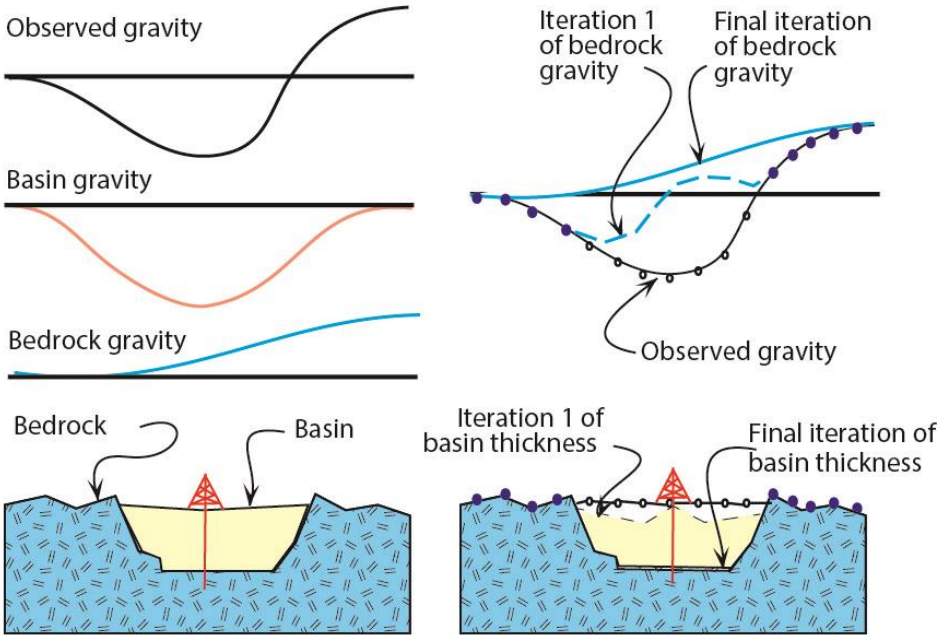

Figure 5. Cartoon showing method to estimate basin thickness (*9*). Blue and white circles indicate locations and anomaly values of gravity measurements on bedrock and basin-fill deposits, respectively.

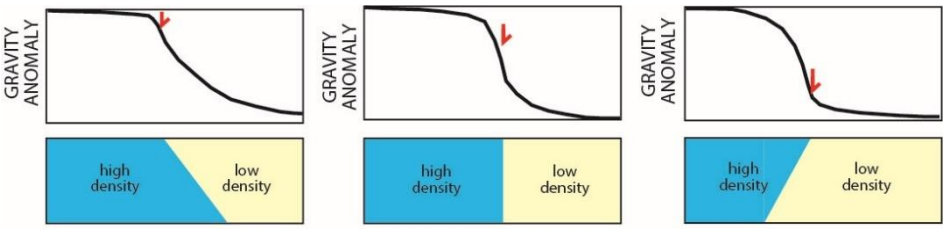

Figure 6. Cartoon showing horizontal gradient method (*10*). The red arrow indicates the maximum horizontal gravity gradient. If the maximum horizontal gravity gradient falls in the middle of the slope, the contact between high- and low-density material (such as a fault) is vertical. If it is located near the top of the gradient, the dip is towards the right, if at the bottom, the dip is towards the left.

References

1. K. Sieh, L. Jones, E. Hauksson, K. Hudnut, D. Eberhart-Phillips, T. Heaton, S. Hough, K. Hutton, H. Kanamori, A. Lilje, S. Lindvall, S. McGill, J. Mori, C. Rubin, J. Spotila, J. Stock, J.K. Thio, J. Treiman, B. Wernicke, J. Zachariasen, Near-field investigations of the Landers earthquake sequence, April to July 1992. *Science* **260**, 171-176 (1993).
2. J. Treiman, K. Kendrick, W. Bryant, T. Rockwell, S. McGill, Primary surface rupture associated with the Mw 7.1 16 October 1999 Hector Mine earthquake, San Bernardino county, California. *Bull. Seismo. Soc. Am.* **92**, 1171-1191 (2002).
3. K. Olsen, S. Day, J. Minster, Y. Cui, A. Chourasia, M. Faerman, R. Moore, P. Maechling, T. Jordan, Strong shaking in Los Angeles expected from southern San Andreas earthquake. *Geophys. Res. Lett.* **33**, L07305 (2006).
4. J. Caine, J. Evans, C. Forster, Fault zone architecture and permeability structure. *Geology* **24**, 1025-1028 (1996).
5. D. Mabey, Geophysical studies in the intermontane basins in southern California. *Geophysics* **21**, 839-853 (1956).
6. R. Jachens, V. Langenheim, J. Matti, Relationship of the 1999 Hector Mine and 1992 Landers fault ruptures to offsets on Neogene faults and distribution of late Cenozoic basins in the Eastern California Shear Zone. *Bull. Seismo. Soc. Am.* **92**, 1592-1605 (2002).
7. V. Langenheim, S. Biehler, R. Negrini, K. Mickus, D. Miller, R. Miller, Gravity and magnetic investigations of the Mojave National Preserve and adjacent areas, California and Nevada. *U.S.G.S Open-File Rep.* **2009-1117**, 25 p. (2009).
8. R. Blakely, *Potential theory in gravity and magnetic applications* (Cambridge Univ. Press, New York, 1996).
9. R. Jachens, B. Moring, Maps of the thickness of Cenozoic deposits and isostatic gravity over basement for Nevada.

U.S.G.S. Open-File Rep. **90-404**, 15 p. (1990).

10. R. Blakely, R. Simpson, Approximating edges of source bodies from magnetic or gravity anomalies. *Geophysics* **51**, 1494-1498 (1986).
11. V. Langenheim, D. Miller, Connecting the Soda-Avawatz and Bristol-Granite Mountains faults with gravity and aeromagnetic data, Mojave Desert, California in *ECSZ does it*, R. Reynolds Ed. (Calif. State Univ. Des. Sci. Center, 2017), pp. 83-92.
12. U.S. Geological Survey and California Geological Survey, Quaternary fault and fold database of the United States, at https://www.usgs.gov/natural-hazards/earthquake-hazards/faults accessed Feb. 10, 2012.
13. D. Miller, S. Dudash, H. Green, D. Lidke, L. Amoroso, G. Phelps, K. Schmidt, A new Quaternary view of northern Mojave tectonics suggests changing fault patterns during the late Pleistocene. *U.S.G.S. Open-File Report* **2007-1424**, pp. 157-171 (2007).
14. D. Miller, R. Miller, J. Nielsen, H. Wilshire, K. Howard, P. Stone, Geologic map of the East Mojave National Scenic Area, California in Geology and mineral resources of the East Mojave National Scenic Area, San Bernardino County, California, T. Theodore Ed., *U.S.G.S. Bulletin* **2160** (2007).
15. C. Jennings, R. Strand, T. Rogers, Geologic map of California. Calif. Div. Min. Geol., scale 1:750,000 (1977).

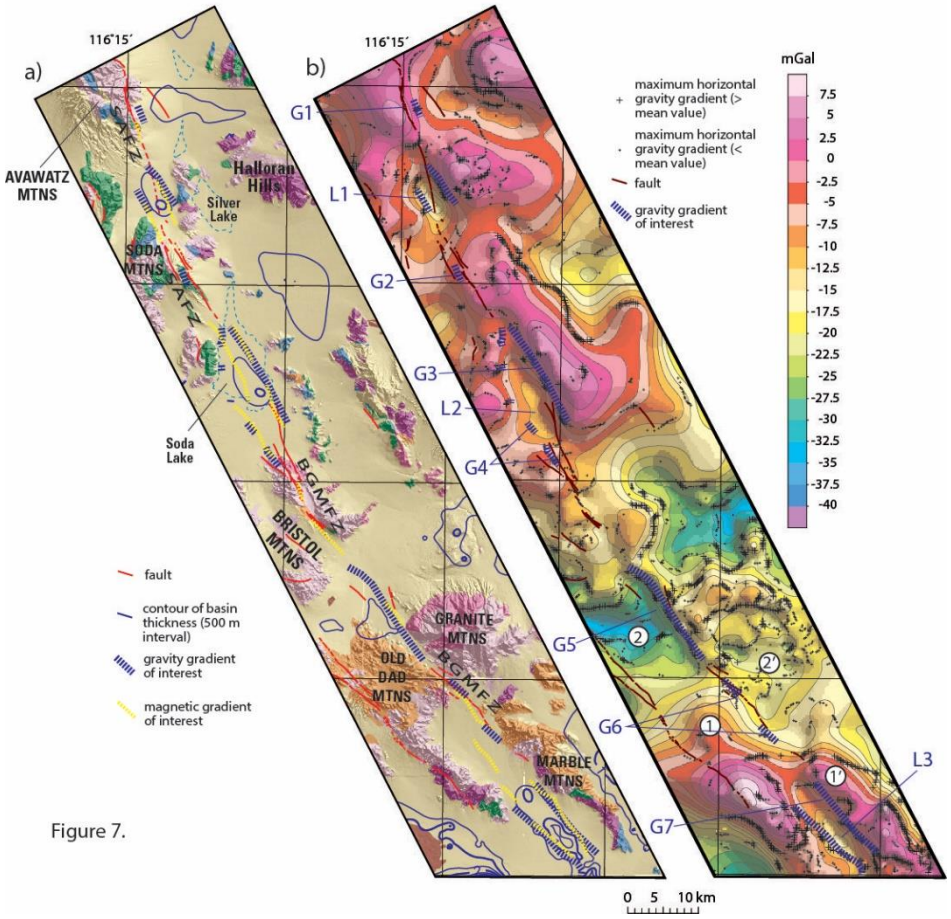

Figure 7.

Figure 7. a) Simplified geologic map (*14, 15*) draped on shaded-relief topography illustrating interpretation of concealed map strands connecting the Soda-Avawatz and Bristol-Granite Mountains fault zones (SAFZ and BGMFZ, respectively) based on gravity gradients (*11*). b) Isostatic gravity anomaly map of the same area with gravity gradients, gravity lows, and other features of interest. Matching gravity high-low pairs (1 and 2) on the left side of the fault with those on the right side of the fault (1' and 2') suggests about 15-17 km of right-lateral displacement.

A Suntan Effect in the Mojave Desert Moss *Syntrichia caninervis*

Jenna T. B. Ekwealor [1]

When you think of moss, you probably picture green, small, maybe even fuzzy, plants growing on bricks and the north side of tree trunks. You probably are not picturing the black crusty stuff on the sand in the desert. While many mosses are indeed found in cool, low-light environments, several species are actually abundant in deserts, including in Mojave National Preserve. Mosses are non-vascular plants that are poikilohydric, meaning their tissues quickly equilibrate to ambient water content, which, by definition, is frequently low in deserts. Desert mosses will completely dehydrate and shut down all metabolic activity between rare precipitation events. These plants are able to recover and function normally when hydrated again, an ability known as desiccation tolerance (*1*).

Figure 1. Mosses *Syntrichia caninervis* (darker plants) and *Pterygoneurum* sp. (lighter plants) in a Granite Mountains Mojave Desert biological soil crust.

Mosses that live on desert soils are not alone. They live in complex communities called biological soil crusts, or biocrusts, made up of desiccation-tolerant organisms such as mosses, lichens, fungi, algae, and cyanobacteria, that live on the soil surface (*2*). Biocrusts are extremely important in desert ecosystems. For one, they physically hold the soil together and reduce erosion (*3, 4*), thus helping retain soil nutrients in an already nutrient-limited ecosystem. They also increase soil fertility by adding nutrients to the soil (*5*) and, in some cases, by increasing water infiltration (*3, 6*). Together, these functions can facilitate germination of native seeds (*7–9*) while reducing germination of exotic seeds (*10*).

The highly desiccation-tolerant (*11, 12*) moss *Syntrichia caninervis* occurs frequently in Mojave biocrusts where it plays important roles (*13*). Biocrust mosses contribute to soil formation and stability with their root-like structures called rhizoids (*14*). In some dryland ecosystems, biocrust mosses control the overall carbon balance by reaching peak photosynthetic activity during winter months when surrounding shrubs may be dormant (*15, 16*). While the functions provided by biocrust mosses in general have become more understood, less is known about the physiology of specific dominant biocrust mosses such as *S. caninervis*, especially in regard to how they tolerate solar radiation while dry.

Mojave National Preserve biocrust organisms, including mosses, spend most of their time in the desiccated state where they are exposed to high temperatures and intense solar radiation (*17*). While dry, they have no metabolic activity (*18*) and, thus, no ability to actively protect themselves or to repair damage. Desiccated desert mosses and other organisms exposed to high intensity UV radiation risk damage to sensitive molecules, including DNA, which absorbs wavelengths in the UV spectrum. Several biocrust cyanobacteria species produce UV-absorbing sunscreens. For example, the sunscreen pigment scytonemin is a yellow-brown colored molecule in the sheaths surrounding common biocrust species in the genus *Nostoc* (*19, 20*) and it is synthesized in response to UV-B exposure, providing passive protection against the whole UV spectrum (*21*). In high quantities, scytonemin-containing cyanobacteria can give the surface of biocrusts a dark brown or black color. Some lichens also produce UV-sunscreens (*22, 23*) and many in Mojave biocrusts are also darkly pigmented.

Strategies for passive photoprotection in mosses are poorly understood. Mosses lack many of the physical protective structures seen in vascular plants, such as thick, waxy cuticles, which strongly absorb UV radiation (*24*), and thick leaves as most moss leaves are only one cell thick. Yet, what mosses lack in morphological adaptations they may make up for with physiology. In natural habitats, *S. caninervis* develops a dark brown coloration (Figure 1) but when grown in low light conditions, such as in a lab, it remains bright green. This pattern suggests the dark pigmentation may be a photoprotective sunscreen. However, it is unknown what environmental signal induces the pigment synthesis in this species. This study aimed to test the hypothesis that UV radiation induces dark pigmentation in *S. caninervis*, and that removal of UV radiation will result in a brighter green (or less brown/black) coloration.

[1] University of California, Berkeley.

To test for the effects of UV-removal on plants of *S. caninervis* in their natural habitat, a year-long manipulative field experiment using UV-filtering and UV-transmitting acrylic windows was conducted at the Sweeney Granite Mountains Desert Research Center, an ecological reserve of the University of California Natural Reserve System. In June 2018, twenty 12.7 cm x 12.7 cm (5" x 5") UV-filtering windows, 3.175 mm (1/8") thick (OP-3 acrylic, Acrylite, Sanford, ME, USA), were installed over target *Syntrichia caninervis* cushions at the study site (Figure 2). In a paired design, twenty UV-transmitting, but otherwise identical acrylic windows (Polycast Solacryl SUVT acrylic, Spartech, Maryland Heights, MO, USA) were placed over target cushions within 1 m of their UV-filtering counterpart. This design allowed me to test the effects of UV radiation alone and control for any other unintended effects the windows might have, such as on temperature or humidity. The windows were installed using #8-32 threaded nylon legs so that each window was nearly flush with the ground on the south edge and approximately 2.5 cm off the ground on the north edge, creating an approximately 13˚ angle with the soil surface. I monitored and re-secured window installations monthly until I collected samples in June 2019. At that time, one UV-filtering window had been lost to weather and that sample was excluded from later analyses. Sample specimens of approximately 9 cm in diameter were collected from each of the remaining 19 pairs. In addition, to test for effects of a window treatment, an additional third, un-manipulated reference sample was collected from each of the 19 microsites within 1 m of the window pair. After collection, samples were returned to the laboratory where I prepared them for subsequent analyses, including some experiments not presented here. Of the original 19 triplets, just 14 had enough moss remaining for image analysis. From each of these, ten individual shoots were selected and photographed for a total of 420 shoots and 42 images.

Upon observation, mosses that had UV filtered out for a year appeared to be greener than those that had a UV-transmitting window and that were un-manipulated (Figure 3). In order to formally test for differences in color, photographs were first processed in Matlab with the Color Thresholder function from the Image Processing Toolbox (*25*). This first step was to create a function that will automate masking, or removing, the background from all photos (Figure 4). The masking process is not perfect because some of the moss shoots get masked and some of the background is left unmasked; however, this technique allows many images to be processed in a blind, high-throughput way. After masking, the proportion of red, green, and blue pixels were quantified in the statistical software R (*26*). Of particular interest is the proportion green pixels as a lower proportion green may indicate higher quantities of non-green sunscreen pigments. I then compared the proportion green pixels in photos of each treatment and tested for statistically significant differences with pairwise Wilcoxon tests to account for the small sample size (*27*) with a Benjamini-Hochberg correction for multiple tests (*28*). *Syntrichia caninervis* shoots that had UV reduced for a year in their natural habitat had significantly higher proportion green pixels than shoots that had ambient and near-ambient levels of UV (Figure 5).

Figure 2. A UV-filtering window (circled) installed over biological soil crust mosses, next to a California buckwheat, *Eriogonum fasciculatum*.

Accordingly, plants exposed to UV during the study period appeared to have more of the dark brown or black pigmentation that is characteristic of this species. This result suggests that accumulation of this pigment is induced by exposure to UV radiation and it may represent a UV sunscreen. Interestingly, the un-manipulated site reference samples also had a lower proportion of green pixels than those with the UV transmitting window. As site reference samples had no window over them it is possible that they had different temperature, relative humidity, or amounts of precipitation reaching them over the study period. It is possible that UV exposure is not the only environmental factor contributing to dark pigmentation in this species. To help understand this, future research could aim to measure the microclimate of the mosses with and without the windows to test for differences that could affect pigmentation. In addition, it is possible that the small amount of UV radiation that does not pass through the UV-transmitting window is the cause of the differences in pigmentation between UV-transmitting and site reference samples. In fact, there is a nearly 10% reduction in UV radiation for the mosses beneath the UV-transmitting windows, compared to the unmanipulated site reference, because some radiation is reflected off the window. It would be interesting to, in future research, test the hypothesis that this dark pigmentation correlates with UV exposure by using more windows that transmit different amounts of UV radiation.

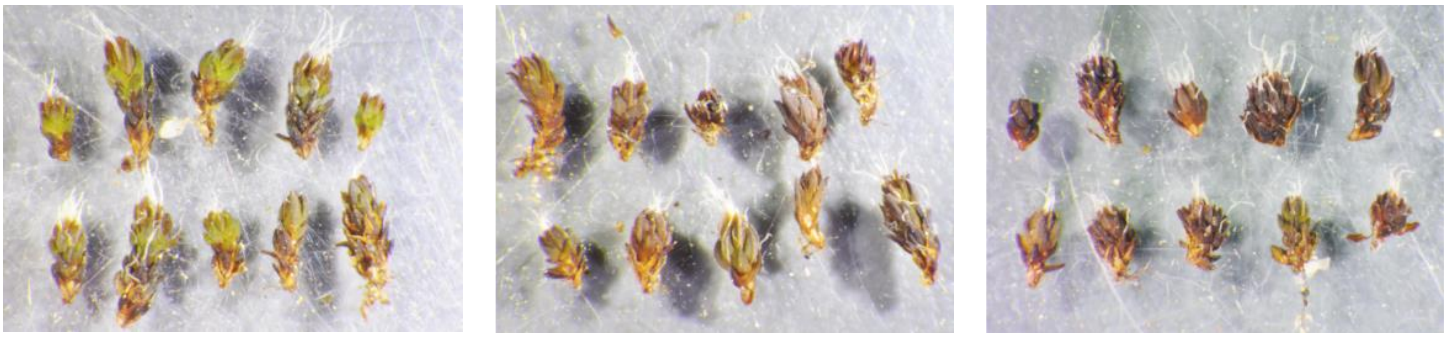

Figure 3. *Syntrichia caninervis* shoots from a UV-filtering window, a UV-transmitting window, and an un-manipulated site reference sample.

It is unclear whether this pigmentation confers protection from UV or whether a reduction in pigmentation will result in a reduction in protection. UV tolerance can be measured in a variety of ways: growth, photosynthetic performance, cell damage, accumulation of UV-absorbing pigments, to name a few. Experiments on mosses have shown that responses to UV vary and is often species-specific. In general, nearly all mosses tested in a field setting appear to be adequately adapted to ambient UV levels based on growth measures but some are damaged by it (*29*). Some species appear to have UV protection regardless of how much UV radiation they're exposed to. For example, in the Antarctic mosses *Sanionia uncinata*, *Chorisodontium aciphyllum*, *Warnstorfia sarmentosa*, and *Polytrichum strictum*, UV-B absorbing compounds are not induced by enhanced UV-B radiation (*29*). On the other hand, in some species, UV protection is induced by UV exposure. For instance, the mosses *Ceratodon purpureus* and *Bryum subrotundifolium*, also from Antarctica, exhibit sun forms that are tolerant to UV and shade forms that are not but can be acclimated to UV within a week in natural sunlight (*30*).

Interestingly, desiccation tolerance appears to correlate with UV-B tolerance in wild grown mosses that were transplanted to a greenhouse and exposed to enhanced UV radiation (*31*). In fact, *S. ruralis*, a close relative of *S. caninervis* and the most desiccation tolerant of the species studied, was not affected by UV-B at all (*31*). It is curious to consider the timing of UV radiation and desiccation stressors for these desert mosses. These plants are desiccated and metabolically inactive when experiencing the most intense radiation and thus, unable to respond to the stressor. They must have adequate protection for summer stressors before summer starts, in other words, before they have experienced the stressor. Instead, they must be able to prepare for a long desiccation period using passive protection, or to have maximum protection all the time. Since UV changes seasonally, it is possible that mosses detect the changes and use it as an indicator to prepare UV sunscreens and other mechanisms of desiccation protection. Further research is necessary to understand the function of the dark pigmentation in *S. caninervis* and its potential role in UV tolerance, and how this might interact with the frequent and prolonged desiccation this species experiences in its natural habitat.

It has been hypothesized that desiccation tolerance is ancestral to land plants and was a crucial step in the colonization of land (*32*). As these desiccated early land plants would have also needed protection from the high UV radiation due to a thin ozone layer, it is possible that passive UV sunscreens are also ancestral to land plants and important in the transition to terrestrial life (*33*). Preliminary results from this experiment indicate that *S. caninervis* is responding to ambient levels of UV radiation. Better understanding of the molecular structure of the pigmentation, the genetic regulation of it, and the role it plays in tolerating intense solar radiation will contribute to the understanding of evolutionary history of land plants as well as of the ecological role of this Mojave Desert biocrust moss.

References

1. B. D. Mishler, A. J. Shaw, B. Goffinet, Bryophyte Biology. *Am. J. Bot.* **88**, 2129 (2001).
2. J. Belnap, The world at your feet : desert biological soil crusts. *Front. Ecol. Environ.* **1**, 181–189 (2003).
3. S. Chamizo, J. Belnap, D. J. Eldridge, Y. Canton, O. Malam Issa, in Biological Soil Crusts: An Organizing Principle in Drylands, *Ecological Studies* **226**, 321–346 (2016).
4. J. Belnap, C. V Hawkes, M. K. Firestone, Boundaries in miniature: Two examples from soil. *Bioscience* **53**, 739–749 (2003).
5. J. Belnap, Nitrogen fixation in biological soil crusts from southeast Utah, USA. *Biol. Fertil. Soils.* **35**, 128–135 (2002).
6. J. Belnap, The potential roles of biological soil crusts in dryland hydrologic cycles. *Hydrol. Process.* **20**, 3159–3178 (2006).
7. C. V. Hawkes, Effects of biological soil crusts on seed germination of four endangered herbs in a xeric Florida shrubland during drought. *Plant Ecol.* **170**, 121–134 (2004).
8. Y.-G. Su, X.-R. Li, Y.-W. Cheng, H.-J. Tan, R.-L. Jia, Effects of biological soil crusts on emergence of desert vascular plants in North China. *Plant Ecol.* **191**, 11–19 (2007).
9. X. R. Li, X. H. Jia, L. Q. Long, S. Zerbe, Effects of biological soil crusts on seed bank, germination and establishment of two annual plant species in the Tengger Desert (N China). *Plant Soil.* **277**, 375–385 (2005).
10. R. R. Hernandez, D. R. Sandquist, Disturbance of biological soil crust increases emergence of exotic vascular plants in California sage scrub. *Plant Ecol.* **212** (2011).

11. A. J. Wood, The nature and distribution of vegetative desiccation-tolerance in hornworts, liverworts and mosses. *Bryologist* **110**, 163–177 (2007).
12. M. C. F. Proctor, M. J. Oliver, A. J. Wood, P. Alpert, L. R. Stark, N. L. Cleavitt, B. D. Mishler, Desiccation-tolerance in bryophytes: a review. *Bryologist* **110**, 595–621 (2007).
13. R. H. Zander, Genera of the Pottiaceae: Mosses of Harsh Environments. *Bull. Buffalo Soc. Nat. Sci.* **32**, 1–378 (1993).
14. R. D. Seppelt, A. J. Downing, K. K. Deane-Coe, Y. Zhang, J. Zhang, in *Biological Soil Crusts: An Organizing Principle in Drylands, Ecological Studies* **226**, B. Weber, B. Büdel, J. Belnap, Eds. (Ecological., 2016; https://doi.org/10.1007/978-3-319-30214-0_6), pp. 101–120.
15. E. Zaady, U. Kuhn, B. Wilske, L. Sandoval-Soto, J. Kesselmeier, Patterns of CO2 exchange in biological soil crusts of successional age. *Soil Biol. Biochem.* **32**, 959–966 (2000).
16. R. L. Jasoni, S. D. Smith, J. A. Arnone, Net ecosystem CO2 exchange in Mojave Desert shrublands during the eighth year of exposure to elevated CO2. *Glob. Chang. Biol.* **11**, 749–756 (2005).
17. S. B. Pointing, J. Belnap, Microbial colonization and controls in dryland systems. *Nat. Rev. Microbiol.* **10**, 654 (2012).
18. B. J. Derek, T. A. Thorpe, On the metabolism of *Tortula ruralis* following desiccation and freezing: Respiration and carbohydrate oxidation. *Physiol. Plant.*, 1399-3054 (1974).
19. P. J. Proteau, W. H. Gerwick, F. Garcia-Pichel, R. Castenholz, The structure of scytonemin, an ultraviolet sunscreen pigment from the sheaths of cyanobacteria. *Experientia* **49**, 825–829 (1993).
20. F. Garcia-Pichel, N. D. Sherry, R. W. Castenholz, Evidence for an ultraviolet sunscreen role of the extracellular pigment scytonemnin in the terrestrial cyanobacterium *Chiorogloeopsis* sp. *Photochem. Photobiol.* **56**, 17–23 (1992).
21. M. Ehling-Schulz, W. Bilger, S. Scherer, UV-B-induced synthesis of photoprotective pigments and extracellular polysaccharides in the terrestrial cyanobacterium *Nostoc* commune. *J. Bacteriol.* **179**, 1940–1945 (1997).
22. F. Lohezic-Le Devehat, B. Legouin, C. Couteau, J. Boustie, L. Coiffard, Lichenic extracts and metabolites as UV filters. *J. Photochem. Photobiol. B Biol.* **120**, 17–28 (2013).
23. F. Rancan, S. Rosan, K. Boehm, E. Fernández, M. E. Hidalgo, W. Quihot, C. Rubio, F. Boehm, H. Piazena, U. Oltmanns, Protection against UVB irradiation by natural filters extracted from lichens. *J. Photochem. Photobiol. B Biol.* **68**, 133–139 (2002).
24. P. Krauss, C. Markstadter, M. Riederer, Attenuation of UV radiation by plant cuticles from woody species. *Plant Cell Environ.* **20**, 1079–1085 (1997).
25. MATLAB, 9.8 (R2020a) (The MathWorks Inc., Natick, Massachusetts, 2020).
26. R Core Team, R: A language and environment for statistical computing (2019), (available at https://www.r-project.org/).
27. F. Wilcoxon, Wilcoxon ranking test for

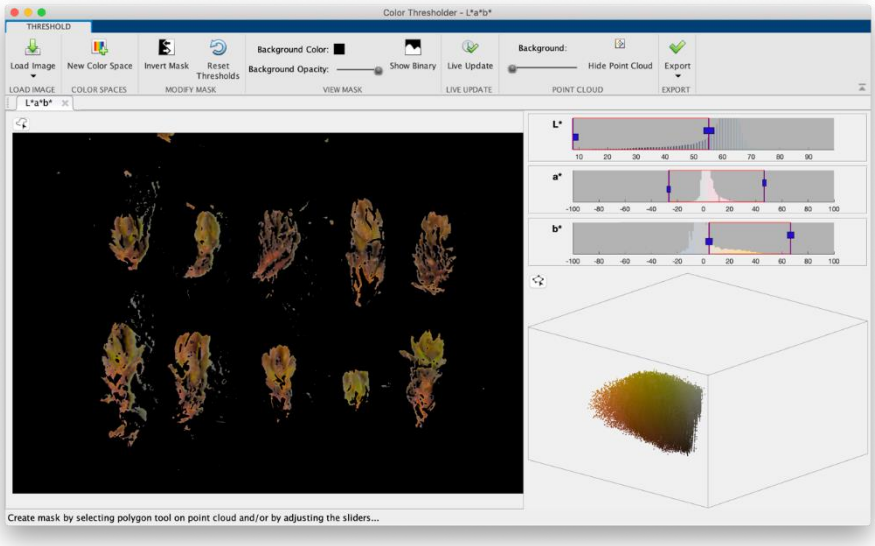

Figure 4. Matlab Color Thresholder from the Image Processing Toolbox masking out background pixels on a photo of *Syntrichia caninervis* shoots.

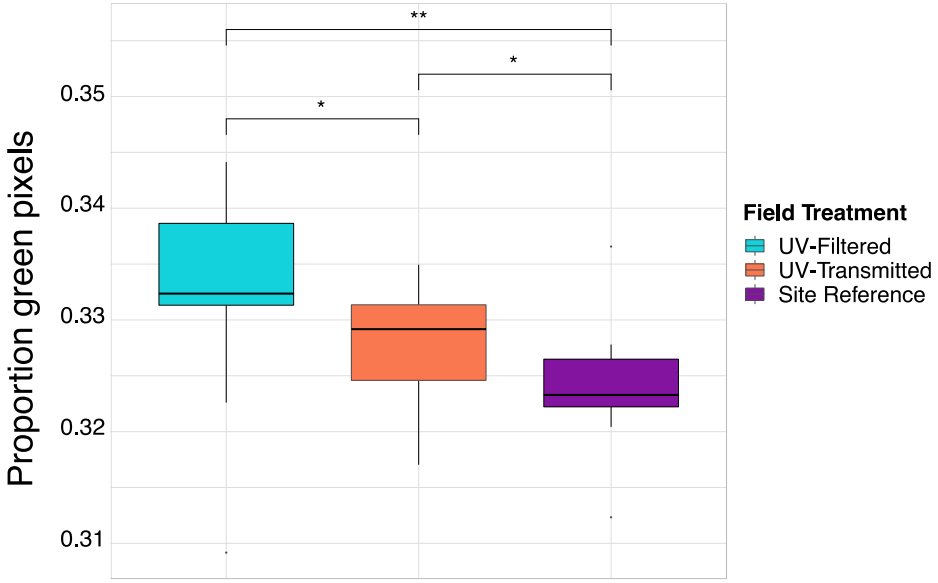

Figure 5. Boxplot showing proportion green pixels in photos of UV-filtered, UV-transmitted, and un-manipulated site reference Syntrichia caninervis shoots. Significance reported for pairwise Wilcoxon tests with Benjamini-Hochberg correction. * P < 0.05, ** P < 0.01.

unpaired measurements. *Biometrics Bull.* **1**, 80 (1945).
28. Y. Benjamini, Y. Hochberg, Controlling the False Discovery Rate: A Practical and Powerful Approach to Multiple Testing. *J. R. Stat. Soc. Ser. B.* **57**, 289–300 (1995).
29. P. Boelen, M. K. De Boer, N. V. J. De Bakker, J. Rozema, Outdoor studies on the effects of solar UV-B on bryophytes: Overview and methodology. *Plant Ecol.* **182**, 137–152 (2006).
30. T. G. A. A. Green, D. Kulle, S. Pannewitz, L. G. Sancho, B. Schroeter, UV-A protection in mosses growing in continental Antarctica. *Polar Biol.* **28**, 822–827 (2005).
31. Z. Takács, Z. Csintalan, L. Sass, E. Laitat, I. Vass, Z. Tuba, UV-B tolerance of bryophyte species with different degrees of desiccation tolerance. *J. Photochem. Photobiol. B Biol.* **48**, 210–215 (1999).
32. M. J. Oliver, Z. Tuba, B. D. Mishler, The evolution of vegetative desiccation tolerance in land plants. *Plant Ecol.* **151**, 85–100 (2000).
33. M. M. Caldwell, Plant life and ultraviolet radiation: Some perspective in the history of Earth's UV climate. *Bioscience* **29**, 520–525 (1979).

Interesting Animal Sightings

An unusual sighting in the fall of an American Badger (*Taxidea taxus*) at the Granite Mountains. The burrows of these animals are easily distinguished by their round openings and mound of dirt created by their impressive claws while digging. We frequently see the burrows scattered throughout the area; however, we don't often see the badgers. Photo by Tasha La Doux, October 19, 2020.

Rock Wren (*Salpinctes obsoletus*) fledglings emerging from a rock crevice in the Granite Mountains. These grayish brown songbirds can be found year-round in the Mojave Desert and are best identified by their bobbing behavior as they perch on rocks. Photo by Malory Owen, May 8th, 2019.

Editors:

Debra Hughson
Mojave National Preserve

Tasha La Doux and James André
Sweeney Granite Mountains Desert Research Center

The Science Newsletter is produced and published by Sweeney Granite Mountains Desert Research Center and the Division of Science and Resource Stewardship, Mojave National Preserve, National Park Service.

Archived at:

http://www.nps.gov/moja/learn/science-newsletter.htm

The Dome Fire

Drew Kaiser [1] and Debra Hughson [1]

A dry lightning strike ignited the Dome Fire in Mojave National Preserve at 1522, August 15, 2020. Over the course of the next few days it burned approximately 43,273 acres, primarily in Joshua tree forest on Cima Dome (Figure 1). Engine 3631 responded from Hole in the Wall Interagency Fire Center and was on scene by 1700, assisted by Brush Engine 53 from Baker and San Bernardino County. Initial requests for aircraft were denied due to the extremely active fire season. Windy conditions on August 16 drove the fire in multiple directions. The fire jumped Cima Road northward, burning most of the historic Kessler Springs Ranch. Authority was transferred August 17 to California Fire Incident Management Team 12 and the National Park Service authorized retardant drops to protect historic structures in the Standard Mining District. The fire was 100% contained August 24 after burning an estimated 1.3 million Joshua trees (*Yucca brevifolia* var. *jaegeriana*). Eleven historic structures were damaged or destroyed. Energy Release Component (ERC) values recorded at the nearby Mid Hills Remote Automatic Weather Station had been at the long-term 97-percentile over the past month and had reached near record highs during the preceding two weeks.

[1] National Park Service, Mojave National Preserve.

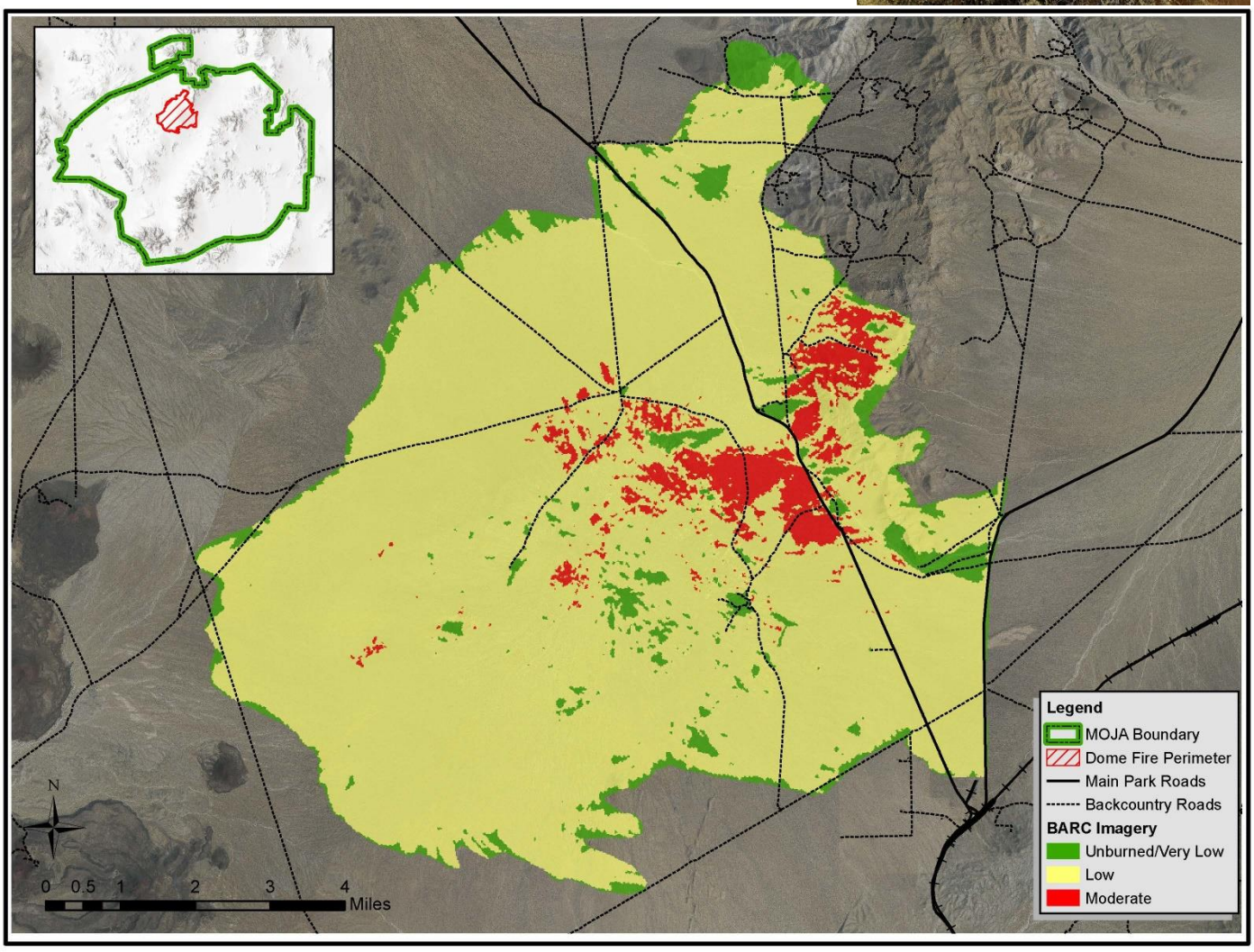

Figure 1. Burned Area Reflectance Classification (BARC) provides a projection of the soil burn severity from pre- and post-fire Landsat imagery. BARC does not capture detailed vegetation mortality in arid systems. It is a qualitative post-fire assessment.